Research Article | Vol. 27, No. 3 | 4 Feb 2019 | OPTICS EXPRESS 3284
Optics EXPRESS

X-ray computational ghost imaging with single-pixel detector

Y. KLEIN,[1] A. SCHORI,[1] I. P. DOLBNYA,[2] K. SAWHNEY,[2] AND S. SHWARTZ[1,*]

[1]*Physics Department and Institute of Nanotechnology and advanced Materials, Bar-Ilan University, Ramat Gan, 52900, Israel*
[2]*Diamond Light Source Ltd, Harwell Science & Innovation Campus, Didcot, Oxfordshire OX11 0DE, UK*
[*]*sharon.shwartz@biu.ac.il*

Abstract: We demonstrate computational ghost imaging at X-ray wavelengths with only one single-pixel detector. We show that, by using a known designed mask as a diffuser that induces intensity fluctuations in the probe beam, it is possible to compute the propagation of the electromagnetic field in the absence of the investigated object. We correlate these calculations with the measured data when the object is present in order to reconstruct the images of 50 μm and 80 μm slits. Our results open the possibilities for X-ray high-resolution imaging with partially coherent X-ray sources and can lead to a powerful tool for X-ray three-dimensional imaging.

1. Introduction

X-ray imaging techniques are widely used in a variety of fields ranging from basic science and high-tech industry to medicine and homeland security. The main advantages of the X-rays are the extremely high spatial resolution, the strong dependence on atom species and densities, and the relatively long penetration depth compared to electrons, which are commonly used for high-resolution imaging.

Despite the existence of many instruments and devices, which are based on X-ray imaging, there are several physical limitations that restrict the resolution and contrast of these techniques. The main fundamental challenge in X-ray imaging is the absence of high quality lenses because of their small magnification and aperture size. It is therefore desired to develop X-ray imaging techniques that do not require lenses and provide high quality images with high resolution and high contrast. Indeed, many techniques and approaches for lensless imaging have been demonstrated with various degree of success [1–5], but none of them has become an ultimate method for imaging. Although some of the techniques have been proven to be very successful in imaging of nanoscale objects [1–4], they require high coherence and therefore are suitable only to synchrotron beamlines with high coherence or to X-ray free-electron lasers.

Ghost imaging (GI) and ghost diffraction (GD) are imaging techniques that have been proven to be applicable even with low coherence sources [6,7]. They have been investigated mainly in the optical regime [7–22] and recently several very significant publications have demonstrated the effects with X-rays [23–29]. In addition of being methods that can be implemented with incoherent sources, GI and GD can lead to imaging methods with very low dose [28] and to imaging of objects in turbid media [14–16]. The later can lead to imaging of biological samples in their natural environment.

In the conventional schemes, GI and GD with partially coherent sources are implemented by introducing fluctuations into the beam by a rotating diffuser and then splitting the beam into two beams with identical intensity fluctuations. One of the beams impinges on the object and is detected by a single-pixel detector while the other beam is detected by a multi-pixel

#352710 https://doi.org/10.1364/OE.27.003284
Journal © 2019 Received 27 Nov 2018; revised 28 Dec 2018; accepted 29 Dec 2018; published 30 Jan 2019

Optics EXPRESS

detector that is blind to the object. In GI, the single-pixel detector is adjacent to the object while in GD the single-pixel detector is mounted far from the object and the distances between the two detectors to the beam splitter are equal. After making many repetitions (realizations) of the process for different positions of the diffuser, the correlation measurements between the two beams are used to reconstruct either the image in the case of GI or the intensity of the diffraction pattern of the object in case of GD. In another scheme for GI [23,28], a moving diffuser is also used to introduce intensity fluctuations, but the spatial distributions of the intensities at the multi-pixel detector for the various configurations of the diffuser are measured first in the absence of the object. These distributions of the intensity are recorded and then the object is inserted into the beam and a single-pixel detector is used to measure the intensities for the same configurations of the moving diffuser. In the last step, the correlations between the two measurements are computed and used to reconstruct the image. In this scheme the beam splitter is not required, but it is still necessary to use the multi-pixel detector in the first step.

A method that requires only one single-pixel detector and no beam splitters has several important advantages with respect to the other methods and can be used to overcome several of the fundamental challenges in the other approaches. In particular, single-pixel detectors are faster, cheaper, and easier to use than multi-pixel detectors. In the conventional scheme for GI and GD, the beam splitter adds different intensity fluctuations to each of the beams and therefore reduces the signal-to-noise ratio [25]. In addition, it is very challenging to find X-ray beam splitters with equal reflectance and transmission and with negligible loss, thus the contrast of the image is limited [25]. In the other approach without the beam splitter [23,28] the resolution and the field of view are limited by the pixel size and the number of pixels of the multi-pixel detector. These limitations can be lifted by using only one single pixel detector. Another significant advantage of imaging with a single-pixel detector is the relatively small amounts of data that are recorded in comparison with multi-pixel detectors. This advantage could be extremely important for measurements that require three or more dimensional imaging.

Interestingly, a method that implements GI with only one single-pixel detector, which is known as computational ghost imaging (CGI, or for ghost diffraction CGD), has been proposed theoretically by Shapiro [13] and demonstrated with optical radiation [16–21]. The basic concept is to replace the diffuser with an unknown scatter distribution by a diffuser with a known scatter distribution. Since the phase and amplitude fluctuations that are induced by the diffuser are known, it is possible to use the Fresnel-Huygens propagator to compute the intensity profile at the detector for each of the realizations thus this procedure does not require a multi-pixel detector. In the last step, the calculated intensity distributions are correlated with the measured intensities at the single-pixel detector that is placed behind the object and the image is reconstructed from the computed correlations. In the optical regime the diffuser is typically implemented by using a spatial light modulator (SLM) [17–19] or a digital micro-mirror device [20,21], but at X-ray wavelengths similar devices are not available. Consequently, the implementation of CGI with X-rays requires a different approach.

Here we present the demonstration of CGI with one single-pixel detector at X-ray wavelengths. We design masks, which are based on numerical simulations we performed, and are fabricated by nanotechnology techniques. We demonstrate the imaging of 50 μm and 80 μm slits at a resolution of about 10 μm with two different masks.

2. CGI procedure

The calculation procedure relies on the derivation of CGI by Shapiro [13], but in our procedure we substitute the SLM by a mask made by photolithography. The main difference between the experiment we describe here and the proposal made by Shapiro in [13] is that the source, which impinges upon the mask in our experiment is partially coherent where the

Optics EXPRESS

spatial coherent length is on the order of the speckle size, while Shapiro considered a scenario where the beam that illuminates the SLM is completely coherent. Consequently, we extend the procedure of Shapiro to partially coherent sources as we elaborate below.

Since we know the thickness of the mask at each position, we can calculate the two-dimensional transmission function U(x,y) by using the tabulated data for X-ray indices of refraction and absorption coefficients [30]. Here x and y are the coordinates across the mask. The mask pattern is designed so that at each of the realizations, the beam hits a small portion of the mask where the variations are only along the x axis. Therefore, we define the one-dimensional transmission function for every realization r as:

$$U_r(x) = B_r(x)e^{i\varphi_r(x)} \tag{1}$$

Here $\varphi_r(x)$ and $B_r(x)$ are the phase that the mask introduces to the beam and the square root of the intensity transmission of the mask, respectively, at each position x. Once we know the electric field after the mask, we can calculate the intensity distribution at the plane of the object, which is at a distance z from the mask, by using the Huygens-Fresnel propagator:

$$I_{C_r}(x',z) = \left| \int dx E_{in}(x) U_r(x) e^{\frac{ik}{2z}(x-x')^2} \right|^2 \tag{2}$$

Here $E_{in}(x)$ is the electric field before the mask, k is the wave vector, and x' is the coordinate across the plane of the object.

Since the source is partially coherent we use a model where we express E_{in} as:

$$E_{in}(x) = \int_0^{T_d} dt\, A e^{i(kx-\omega t+\phi(x,t))} \tag{3}$$

Here A is the field amplitude, ω is the angular frequency, and T_d is the integration time of the detector. $\phi(x,t)$ is a random temporal and spatial phase function, which is extracted according to the Van Cittert-Zernike theorem [31] from a Gaussian distribution such that the two point correlation function is limited by the coherence volume of the field. The spatial coherence length in our experiment can be evaluated by using [31] $\sigma_l \approx \lambda/\theta$ where λ is the wavelength and θ is the divergence angle to be several microns. The temporal coherence length is about a femtosecond and is determined by the bandwidth of the input monochromator.

We denote the transmission function of the object as T(x'). The intensities at the single-pixel detector that is mounted immediately after the object are given by $I_{B_r} = \int dx' I_{C_r} T(x')$. I_{B_r} is cross-correlated with the computed intensity patterns I_{C_r} and after N realizations the image can be reconstructed by using the second-order-intensity correlation function:

$$G(x) = \frac{1}{N}\sum_{r=1}^{N}\left(I_{B_r} - \langle I_B \rangle\right) I_{C_r} = \langle I_B I_C \rangle - \langle I_B \rangle \langle I_C \rangle \tag{4}$$

The $\langle \cdot \rangle$ indicates an ensemble average over the realizations, where each of the realizations refers to a different position on the mask and therefore represents different intensity and phase fluctuations.

3. Experimental setup

We conducted the experiments described below at beamline B16 of Diamond Light Source [32]. The schematic of the experimental system is shown in Fig. 1(a). The distance between the mask and the object is 100 mm and the detector is mounted immediately behind the

Optics EXPRESS

object. We use a monochromatic X-ray beam at 11 keV. The divergence angle is about 0.2 mrad and the relative spectral bandwidth ΔE/E is about 10^{-4} (achieved by using a Si(111) monochromator). The beam with a spot size of 800 μm x 200 μm at full width half maximum (FWHM) hits a selected area of the diffuser and propagates according to the pattern in that specific portion. Next, the beam passes through the object and it is collected by the single-pixel detector, which we mount behind the object.

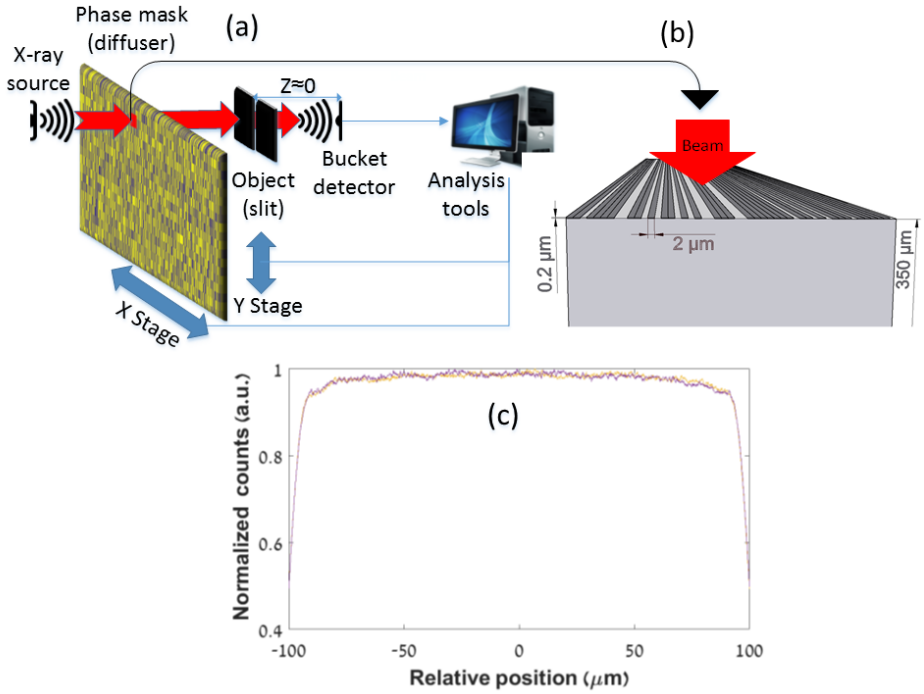

Fig. 1. (a) Schematic of the computational ghost imaging experimental setup. A diffuser is mounted on linear stages. The beam hits a small portion of the diffuser, then it propagates through the object and is detected by a single-pixel detector mounted as close as possible to the object. (b) An example of an illuminated area of mask 2, which is a random pattern of long rectangles with dimensions of 2 μm x 0.2 μm. The pattern changes only in x axis. (c) Two examples of calculated diffraction patterns for two different realizations.

We measured the intensity at the detector for different positions across the mask. We correlate the measured intensities at the detector with the calculations of the free space propagation by using the procedure described in the previous section.

We test two different masks, for the diffusers, which are produced by direct laser lithography. The masks consist of random patterns of metal rectangles on a glass substrate. These features introduce a phase shift of about 0.05π and absorption of about 2%. The specifications of the two masks are summarized in Table 1. An example of one projection area on the second mask is shown in Fig. 1(b), and two examples of calculated diffraction pattern are shown in Fig. 1(c).

Table 1. Specifications of the phase masks

Mask number	Substrate material	Substrate thickness [μm]	Feature material	Feature thickness [μm]	Minimum feature size [μm]	Mask area [cm^2]
1	Quartz	~1500	Iron oxide	0.26 ± 0.03	1 ± 0.05	~100
2	Quartz	~350	Chromium	0.2 ± 0.02	2 ± 0.2	~78.5

Optics EXPRESS

The objects we measure are 50 μm and 80 μm slits, which are implemented by using a one-dimensional motorized slit with a controllable size. The detector is an avalanche photo-diode (APD).

We use the ring current of the synchrotron to filter out the slow temporal fluctuations, the decay, and the filling of the synchrotron beam. We measure the beam profile to normalize the image and to filter out spatial noises. The raw measured data include a spatial high frequency noise that we assume is caused mainly by artifacts in the fabrication of the masks. We filter out this noise by applying a low pass filter in the data analysis process.

We perform the measurements for three combinations of different masks and objects as we summarize in Table 2.

Table 2. Parameters of the CGI experiments

Object size [μm]	Mask number	Average counts per realization	Number of realizations	Measured relative intensity fluctuations [%]
50	2	$\sim 7 \cdot 10^7$	$1.8 \cdot 10^3$	0.29
80	2	$\sim 1 \cdot 10^8$	$2.3 \cdot 10^3$	0.14
80	1	$\sim 4 \cdot 10^6$	$1.8 \cdot 10^3$	0.20

4. Results

We first describe the demonstration of CGI with X-rays, which we show in Fig. 2. Figure 2(a) shows the image of a 50 μm slit that is obtained by using mask 2. We find that the FWHM of the image is 51 μm ± 10 μm. Figures 2(b) and 2(c) show images of an 80 μm slit that is obtained by using mask 2 and mask 1, respectively. We find that the FWHM of the images are 78 μm ± 10 μm and 81 μm ± 8 μm respectively. The blue dots are CGI results when the distance between the sequential dots is 2 μm and 1 μm for mask 2 and for mask 1 respectively.

To test the performance of our measurements we compare the slit widths we measure to the slit sizes we set. The spatial resolution of our measurements is determined by the speckle size at the image plane, which is larger than the feature size at the mask plane because of the diffraction of the speckle pattern over the distance between the diffuser and the plane of the object. The precision of the mask position alignment (about ± 2 μm) also affects the resolution. We therefore estimate the resolution of our measurements to be about 10 μm and 8 μm for mask 2 and for mask 1 respectively. In addition, the calibration of the slit, which is not better than 2 microns, introduces additional uncertainties with respect to the expected width and the low pass filter we use in our data analysis also affects the edges of the images. Within these uncertainties, the widths of the slits we measure agree with the widths of the motorized slits that we set. Of importance, we observe the images of the slits only when we use the correct diffuser mask pattern in our calculations of the CGI image.

Optics EXPRESS

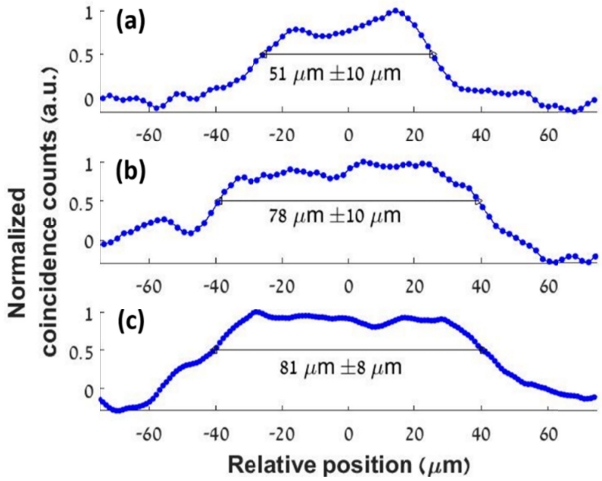

Fig. 2. Experimental results of computational ghost imaging for (a) a 50 μm slit with mask number 2, (b) an 80 μm slit with mask number 2, and (c) an 80 μm slit with mask number 1. The solid lines are guides for the eye.

5. Dependence on the source coherence properties

The source we use to illuminate the mask is partially coherent in contrast to demonstrations of CGI with optical radiation. This major difference leads to the question of how do the image quality and resolution depend on the spatial coherence length of the source?

To answer this question, we simulate the CGI procedure for a 15-micron slit and compare between several spatial coherence lengths and between two types of diffuser masks: a pure phase mask and a pure amplitude mask. We summarize the results of the comparison in Fig. 3. In the upper row (Figs. 3(a)-3(d)) we show the results for the amplitude mask and in the lower row (Figs. 3(e)-3(h)) we show the results for the phase mask. Since the results depend mainly on the ratio between the coherence length and the features size, we define the ratio $R = \sigma_1 / \mathrm{MFS}$, where the MFS is the minimum feature size.

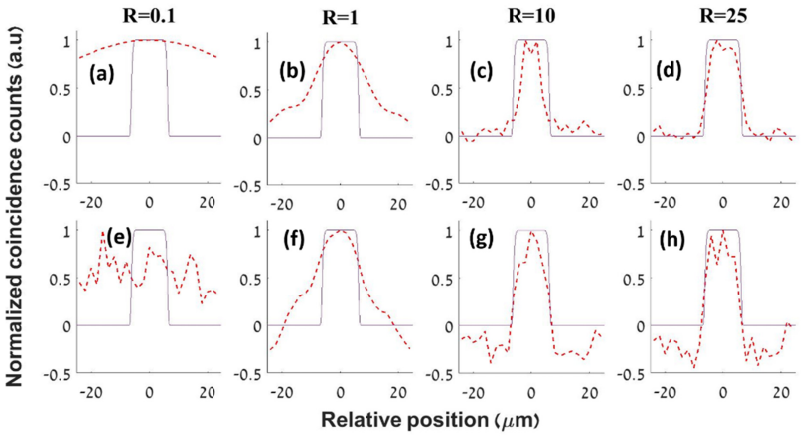

Fig. 3. CGI simulations for several coherent lengths. R is the ratio between the spatial coherence length and the minimum features size of the diffuser. The object is a 15 μm slit (the purple lines are the theoretical slit). In panels (a)-(d) the mask is an amplitude mask and in panels (e)-(h) the mask is a phase mask. The propagation distance we use for the simulations is 100 mm.

Optics EXPRESS

The results in Figs. 3(a)-3(d) indicate that the image can be reconstructed even when the coherence length is smaller than the speckle size if the diffuser is an amplitude mask. However, the resolution improves with the coherence length. For coherence lengths that are shorter than the features size as in Fig. 3(a) the sharp edges of the slits are completely blurred. This is because the divergence angle is inversely proportional to the coherence length (as described in section 2). Since the beam that is scattered from the diffuser expands according to the diffraction angle, the larger the diffraction angle the broader the speckles at the object plane and the resolution decreases.

For the phase mask, the image can be reconstructed only if the coherence length is on the order of the speckles size as in Figs. 3(f)-3(h). We note that in the range where the coherence length is equal or slightly shorter than the feature size of the diffuser, the reconstruction depends strongly on the properties of the partial coherent source model.

In our experiment, the diffuser masks introduce mainly amplitude fluctuations into the beam. Therefore, we conclude that the CGI procedure works, although the coherence length is on the order of the speckle size, and it is possible that the contribution of the phase information is very small. The short coherence length in our case mainly leads to blurring and to the reduction of the spatial resolution, as we show in Fig. 3(b).

In addition, we deduce from the results of Fig. 3 that a larger ratio between the coherence length and the mask feature size could lead to the possibility of using the phase contribution from the mask. This conclusion is important for small objects since the amplitude modulation by the mask is limited by the height of the features of the mask, which are limited by the aspect ratio, which is determined by fabrication limitations. Thus, smaller lateral size of the features has smaller amplitude fluctuations and the addition of the phase fluctuations can enhance the contrast of the reconstructed image.

6. Signal-to-noise ratio and image quality

After we demonstrated the CGI effect and discussed its dependence on the spatial coherence length we turn to quantify the signal-to-noise ratio (SNR) and its dependence on the number of realizations. Theoretically the SNR scales as the square root of the ratio between the number of realizations N and the number of speckles transmitted through the object N_S [33,34]: $\mathrm{SNR} \propto \sqrt{N/N_s}$. Figure 4 shows the SNR as a function of the number of realizations N for CGI results with the 50 μm slit that we show in Fig. 2(a). The black dots are the experimental results and the blue line is an analytic fitting function $a\sqrt{N}$, where "a" is a constant. The SNR matches approximately to the analytical fit and the value of the parameter "a" is 0.5. This result matches to the order of $1/\sqrt{N_S} \propto 10^{-1}$, when N_S is the spot size divided by the feature size. The analysis of the other two experiments yields similar results.

Optics EXPRESS

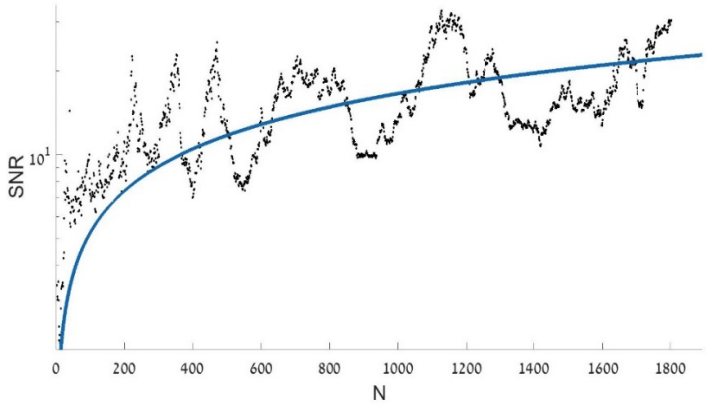

Fig. 4. The SNR as a function of the number of realizations N for CGI results with the 50 μm slit that we show in Fig. 2(a). The black dots are experimental results and the blue solid line is the analytic fitting function a√N. See details in the text.

While the results shown above demonstrate the feasibility of CGI, the quality of the images can be further improved by increasing the thickness of the speckles and hence the amplitude variations that are induced by the diffuser mask. In addition, since the beam diffracts from the mask plane to the image plane, the distance between the diffuser and the object is one of the properties that determines the spatial resolution. Figure 5(a) shows a comparison for CGI of a 50 μm slit (the purple line is the theoretical slit) between the experimental results (blue dotted line), a simulation for the experimental parameters (green dashed line), and a simulation for a mask with transmission variations between 0 and 1 (red dashed line). The results in this panel are obtained by assuming that the object is mounted at the same distance of the experiment (100 mm). Figure 5(b) shows the similar simulations with the exception that the distance between the mask and the object is 30 mm. The coherence length for the simulations is 1 μm.

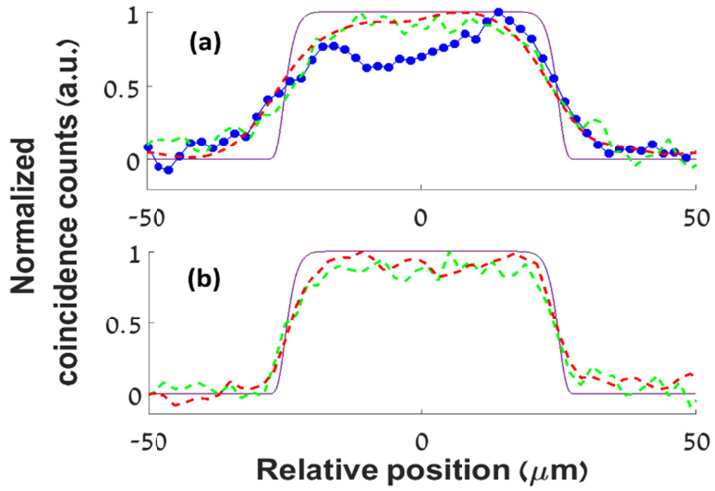

Fig. 5. Comparison between the CGI experimental results (blue dotted line), CGI simulation with the mask that we used in the experiment (green dashed line), and simulation with an ideal mask modulation (red dashed line) for a 50-μm slit (the purple line is the actual shape of the slit). In panel (a) the distance between the diffuser and the object is 100 mm. In panel (b) the distance is 30 mm.

Optics EXPRESS

It is clear that the results of the simulations with the parameters of the experiment (green dashed line) and the experimental results (blue dotted line) in Fig. 5(a) agree within the experimental resolution. However, there is a distortion in the measured image, which is absent in the simulations. Since the calculations in the CGI procedure are based on the information of the mask pattern, we believe that the distortion is caused by inaccuracies in the mask fabrication process.

We note that the resolution of the simulations and the experimental results in Fig. 5(a) are nearly equal. This similarity suggests that the main reason for the limited resolution is the divergence of the beam, and not the experimental errors. Based on this considerations, we anticipate that it would be possible to improve the spatial resolution significantly by moving the object closer to the diffuser as we can see clearly from Fig. 5(b) where the resolution is improved in both simulations (dashed lines). Equivalent ways to improve the resolution are to increase the R factor by using a source with a larger spatial coherence length or by using a mask with smaller features.

We note that the simulations with the ideal mask (red dashed line) show higher SNR. This suggests that it would be possible to improve the SNR of the image by increasing the thickness of the mask features, which will lead to stronger variations of the amplitudes and the phases and a higher correlation function.

7. Conclusion

We have demonstrated the first experimental observation of CGI at X-ray wavelengths with only one single-pixel detector. The simulations we performed suggest that it is possible to improve the SNR, the contrast, and the spatial resolution of the reconstructed images by optimizing parameters such as the aspect ratio and thickness of the speckle size. These improvements can be achieved by using advanced lithography techniques, such as X-ray photolithography [35].

We note that since it is possible to control the parameters of the diffuser by designing an efficient scatter distribution, CGI can also lead to a reduction in the number of realizations that are required for the reconstruction of the images [18,19] and therefore to either shorter measurement durations or to a lower radiation dose that is required for the reconstruction of the images. Furthermore, our method is not limited to near field imaging. By mounting the object far from the detector it would be possible to measure the diffraction pattern of an object [13,17] and to reconstruct the object by a phase retrieval algorithm [22]. In addition, our technique advances the possibilities for three-dimensional imaging [20,21] and for imaging of objects, which are embedded in liquid [16]. Finally, we note that since our technique does not require either high coherence or high brightness, it can be used not just with synchrotron radiation but also with tabletop X-ray sources.

Funding

Israel Science Foundation (ISF) (201/17); EU Framework Program for Research and Innovation HORIZON 2020 (CALIPSOplus under the Grant Agreement 730872).

Acknowledgments

We thank Diamond Light Source for access to Beamline B16 (Proposal No. MT17403), which contributed to the results presented here.

References

1. J. Miao, P. Charalambous, J. Kirz, and D. Sayre, “Extending the methodology of X-ray crystallography to allow imaging of micrometre-sized non-crystalline specimens,” Nature **400**(6742), 342–344 (1999).
2. I. McNulty, J. Kirz, C. Jacobsen, E. H. Anderson, M. R. Howells, and D. P. Kern, “High-resolution imaging by Fourier transform X-ray holography,” Science **256**(5059), 1009–1012 (1992).
3. S. Eisebitt, J. Lüning, W. F. Schlotter, M. Lörgen, O. Hellwig, W. Eberhardt, and J. Stöhr, “Lensless imaging of magnetic nanostructures by X-ray spectro-holography,” Nature **432**(7019), 885–888 (2004).

Optics EXPRESS

4. P. Thibault, M. Dierolf, A. Menzel, O. Bunk, C. David, and F. Pfeiffer, "High-resolution scanning x-ray diffraction microscopy," Science **321**(5887), 379–382 (2008).
5. H. N. Chapman and K. A. Nugent, "Coherent lensless X-ray imaging," Nat. Photonics **4**(12), 833–839 (2010).
6. J. Cheng and S. Han, "Incoherent coincidence imaging and its applicability in X-ray diffraction," Phys. Rev. Lett. **92**(9), 093903 (2004).
7. Y. Cai and S. Y. Zhu, "Ghost imaging with incoherent and partially coherent light radiation," Phys. Rev. E Stat. Nonlin. Soft Matter Phys. **71**(5), 056607 (2005).
8. R. S. Bennink, S. J. Bentley, and R. W. Boyd, ""Two-Photon" coincidence imaging with a classical source," Phys. Rev. Lett. **89**(11), 113601 (2002).
9. J. H. Shapiro and R. W. Boyd, "The physics of ghost imaging," Quantum Inform. Process. **11**(4), 949–993 (2012).
10. P. Ryczkowski, M. Barbier, A. T. Friberg, J. M. Dudley, and G. Genty, "Ghost imaging in the time domain," Nat. Photonics **10**(3), 167–170 (2016).
11. P. A. Morris, R. S. Aspden, J. E. Bell, R. W. Boyd, and M. J. Padgett, "Imaging with a small number of photons," Nat. Commun. **6**(1), 5913 (2015).
12. C. Thiel, T. Bastin, J. Martin, E. Solano, J. von Zanthier, and G. S. Agarwal, "Quantum imaging with incoherent photons," Phys. Rev. Lett. **99**(13), 133603 (2007).
13. J. H. Shapiro, "Computational ghost imaging," Phys. Rev. A **78**(6), 061802 (2008).
14. J. Cheng, "Ghost imaging through turbulent atmosphere," Opt. Express **17**(10), 7916–7921 (2009).
15. R. E. Meyers, K. S. Deacon, and Y. Shih, "Turbulence-free ghost imaging," Appl. Phys. Lett. **98**(11), 111115 (2011).
16. M. Le, G. Wang, H. Zheng, J. Liu, Y. Zhou, and Z. Xu, "Underwater computational ghost imaging," Opt. Express **25**(19), 22859–22868 (2017).
17. Y. Bromberg, O. Katz, and Y. Silberberg, "Ghost imaging with a single detector," Phys. Rev. A **79**(5), 053840 (2009).
18. . M. Mahdi Khamoushi, Y. Nosrati, and S. H. Tavassoli, "Sinusoidal ghost imaging," Opt. Lett. **40**(15), 3452–3455 (2015).
19. W. Chen and X. Chen, "Object authentication in computational ghost imaging with the realizations less than 5% of Nyquist limit," Opt. Lett. **38**(4), 546–548 (2013).
20. B. Sun, M. P. Edgar, R. Bowman, L. E. Vittert, S. Welsh, A. Bowman, and M. J. Padgett, "3D computational imaging with single-pixel detectors," Science **340**(6134), 844–847 (2013).
21. Z. Zhang, S. Liu, J. Peng, M. Yao, G. Zheng, and J. Zhong, "Simultaneous spatial, spectral, and 3D compressive imaging via efficient Fourier single-pixel measurements," Optica **5**(3), 315–319 (2018).
22. R. Borghi, F. Gori, and M. Santarsiero, "Phase and amplitude retrieval in ghost diffraction from field-correlation measurements," Phys. Rev. Lett. **96**(18), 183901 (2006).
23. H. Yu, R. Lu, S. Han, H. Xie, G. Du, T. Xiao, and D. Zhu, "Fourier-transform ghost imaging with hard X rays" Phys. Rev. Lett. **117**(11), 113901 (2016).
24. D. Pelliccia, A. Rack, M. Scheel, V. Cantelli, and D. M. Paganin, "Experimental x-ray ghost imaging," Phys. Rev. Lett. **117**(11), 113902 (2016).
25. D. Pelliccia, M. P. Olbinado, A. Rack, A. M. Kingston, G. R. Myers, and D. M. Paganin, "Towards a practical implementation of X-ray ghost imaging with synchrotron light," IUCrJ **5**(4), 428–438 (2018).
26. A. M. Kingston, D. Pelliccia, A. Rack, M. P. Olbinado, Y. Cheng, G. R. Myers, and D. M. Paganin, "Ghost tomography," Optica **5**(12), 1516–1520 (2018).
27. A. Schori and S. Shwartz, "X-ray ghost imaging with a laboratory source," Opt. Express **25**(13), 14822–14828 (2017).
28. A.-X. Zhang, Y.-H. He, L.-A. Wu, L.-M. Chen, and B.-B. Wang, "Tabletop x-ray ghost imaging with ultra-low radiation," Optica **5**(4), 374–377 (2018).
29. A. Schori, D. Borodin, K. Tamasaku, and S. Shwartz, "Ghost imaging with paired x-ray photons," Phys. Rev. A (Coll. Park) **97**(6), 063804 (2018).
30. B. L. Henke, E. M. Gullikson, and J. C. Davis, "X-ray interactions: photoabsorption, scattering, transmission, and reflection at E= 50-30,000 eV, Z= 1-92," Atom. data Nucl. data **54**(2), 181–342 (1993).
31. J. W. Goodman, *Statistical optics* (Wiley classics library, 2000), Chap. 5.
32. K. J. S. Sawhney, I. P. Dolbnya, M. K. Tiwari, L. Alianelli, S. M. Scott, G. M. Preece, U. K. Pedersen, and R. D. Walton, "A test beamline on diamond light source," in Proceedings of AIP (2010, June), pp. 387–390.
33. B. I. Erkmen and J. H. Shapiro, "Signal-to-noise ratio of Gaussian-state ghost imaging," Phys. Rev. A **79**(2), 023833 (2009).
34. D. Ceddia and D. M. Paganin, "Random-matrix bases, ghost imaging, and x-ray phase contrast computational ghost imaging," Phys. Rev. A (Coll. Park) **97**(6), 062119 (2018).
35. C. Xue, J. Zhao, Y. Wu, H. Yu, S. Yang, L. Wang, W. Zhao, Q. Wu, Z. Zhu, B. Liu, X. Zhang, W. Zhou, and R. Tai, "Fabrication of large-area high-aspect-ratio periodic nanostructures on various substrates by soft X-ray interference lithography," Appl. Surf. Sci. **425**, 553–557 (2017).